Acta Cryst. (1995). A**51**, 831–840

Bragg-Case Images of Stacking Faults

BY W. WIERZCHOWSKI* AND M. MOORE

Department of Physics, Royal Holloway, University of London, Egham, Surrey TW20 0EX, England

(*Received* 17 *November* 1994; *accepted* 12 *June* 1995)

Abstract

Bragg-case synchrotron double-crystal images of stacking faults have been studied in a synthetic diamond. The topographs taken on the tails of the rocking curve showed well pronounced interference fringes arising from the stacking faults: the first such observation in Bragg diffraction geometry. The fringes were strongly dependent upon the angular setting, being invisible at the rocking-curve maximum but gaining in contrast and becoming more closely spaced further from the maximum. These experimental images were compared with predictions of plane-wave dynamical theory and a reasonably good correspondence was obtained when the finite beam divergence was taken into account. It was found that the theoretical fringe sequences depended upon the stacking fault and confirmed that the stacking faults observed were of intrinsic type.

1. Introduction

The interest in studying stacking faults with X-ray topography and electron microscopy has two main motivations. Firstly, stacking faults are important as common crystallographic defects. Secondly, stacking faults provide an opportunity for successful application of the dynamical theory of diffraction for explaining the observed interference fringes. Most X-ray investigations into stacking faults have been by section topography (see *e.g.* Kato, Usami & Katagawa, 1967; Authier, 1968; Jiang & Lang, 1983; Kowalski & Lang, 1986; Kowalski, Lang, Makepeace & Moore, 1989), where spherical-wave theory was applied. The theoretical description of transmission plane-wave diffraction on stacking faults was included in the above-mentioned papers by Authier (1968) and Kato *et al.* (1967) and was also given by Kato (1974).

The observation of interference fringes is usually more difficult in back-reflection diffraction geometry (Bragg case) than in transmission diffraction geometry. To our knowledge, no observations of fringe patterns in stacking-fault images have been reported in the Bragg case. The difficulty in obtaining such fringes is associated with the attenuation of X-rays, reducing the thickness of the layer capable of contributing to interference effects. In addition, interference fringes are expected only on the tails of the rocking curve and, in view of their strong angular dependence, can be observed only with good collimation of the incident beam. Some interference fringes were observed in the Bragg-case plane-wave images of dislocations (Bubáková & Šourek, 1976; Bedyńska, Bubáková & Šourek, 1976; Gronkowski, 1980) and there is still considerable interest in studying Bragg-case interference fringes associated with other defects.

A very convenient material for obtaining interference fringes in stacking-fault images is diamond. It is composed of atoms with very low atomic number and it absorbs X-rays less than most other crystals. Stacking faults are common in diamond and can easily be found in otherwise good-quality crystals. The recent development of the reconstitution method for growing large diamonds (Strong & Wentorf, 1972; Burns, Robertson & Keddy, 1993) has enabled samples suitable for such experiments to be readily available.

In the present work, we obtained Bragg-case images of stacking faults using double-crystal arrangements with a synchrotron source of X-rays. The experimental images were compared with theoretical images obtained from a simple adaptation of former plane-wave approaches to the Bragg case, which also included the effects of incident-beam divergence.

Some results of actual work were presented at the International School on Synchrotron Radiation in Natural Science held in Jaszowiec and published elsewhere (Wierzchowski & Moore, 1992).

2. Theoretical

The back-reflection images of stacking faults can be classified as corresponding to either Bragg–Laue or Bragg–Bragg cases. In the first of these cases, the part of the crystal behind the stacking fault produces the diffracted beam intersecting it, while in the Bragg–Bragg case the beam is reflected back towards the first region of the crystal. We concentrate here on the Bragg–Laue case. (In our present experiments, we observed fringes in the images corresponding also to the Bragg–Bragg case and they will be the subject of further studies.)

The multiplication of wave fields at the stacking fault in the Bragg–Laue case is shown in Fig. 1, while the

* Permanent address: Institute of Electronic Materials Technology, Wólczyńska 133, 01-919 Warsaw, Poland.

ISSN 0108-7673

position of the wave points corresponding to the excited wave fields is shown in Fig. 2. Both figures correspond to the low-angle tail of the rocking curve. At the high-angle side, the indices 1 are replaced by indices 2 and *vice versa*.

We found it reasonable to assume that only one wave point is excited by the incident wave. It should, however, be mentioned that complete elimination of interference effects due to the beam reflected from the rear surface requires more than 40× attenuation of that beam. At the low-angle side of the rocking curve, this assumption may not be entirely appropriate with the present thickness (0.7 mm) of the diamond slab. In actual experiment, negligibility of the second wave was due both to its absorption and to the imperfections in the crystal, which played a significant rôle because of the relatively long distance travelled by the wave reflected from the rear surface. The other possible factor was the preparation of the rear surface, which also caused losses in the internally reflected wave.

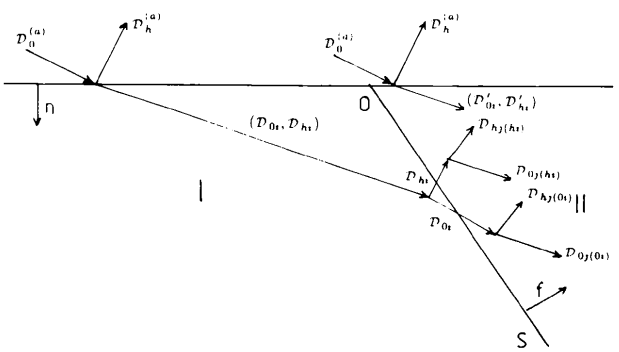

Fig. 1. Wave multiplication at a stacking fault (OS) in the Bragg–Laue case of diffraction. The incident plane wave of amplitude $D_0^{(a)}$ and wave number K excites in the first part of the crystal a single wave field consisting of the waves D_{0i}, D_{hi} with $i = 2$ for the low-angle side of the rocking curve ($\Re y > 1$) and $i = 1$ for the high-angle side ($\Re y < -1$). The two wave fields are decomposed in the fault plane into waves in the transmitted and reflected directions. In region II, each of these waves generates two wave fields (four waves). The amplitudes of these waves are denoted by $D_{0j(0i)}$, $D_{hj(0i)}$, $D_{0j(hi)}$ and $D_{hj(hi)}$ with $j = 1, 2$ and subscripts in parentheses indicating the exciting beam.

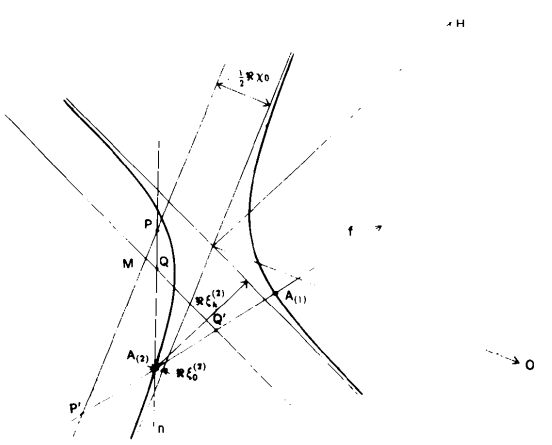

Fig. 2. Positions of the wave points on the dispersion surfaces. Situations correspond to the low-angle tail of the rocking curve. The single wave point excited primarily in the first region $A_{(2)}$ is located on the normal to the entrance surface. The Poynting vector connected with this point is directed inwards towards the crystal. One of the points excited in the second part of the crystal coincides with this point, while the second point $A_{(1)}$ is located on the second branch of the dispersion surface on the normal to the fault plane passing through $A_{(2)}$.

The coordinates of the wave point excited by the incident beam are

$$\xi_0^{(i)} = \tfrac{1}{2}|C|K(\gamma_0/|\gamma_h|)^{1/2}(\chi_h\chi_{\bar{h}})^{1/2}[y \pm (y^2-1)^{1/2}], \tag{1}$$

where K is the wave number of the incident wave, χ_0, χ_h, $\chi_{\bar{h}}$ are the Fourier coefficients of dielectric susceptibility, C is the polarization factor and γ_0, γ_h are the direction cosines of the incident and reflected beams with respect to the normal to the entrance surface.

$$y = -[\sin 2\Theta\Delta\Theta + \tfrac{1}{2}\chi_0(1-\gamma_h/\gamma_0)] \times [|C|(|\gamma_h|/\gamma_0)^{1/2}(\chi_h\chi_{\bar{h}})^{1/2}]^{-1} \tag{2}$$

with $\Delta\Theta$ the deviation from the Bragg angle Θ. $i = 1$ and the upper sign is valid for $\Re y < -1$ ($\Re$ denotes the real part of y) and $i = 2$ and the lower sign is valid for $\Re y > 1$.

The ratios of the reflected amplitude D_{hi} to the amplitude D_{0i} of the forward-diffracted wave are given by

$$c^{(i)} = D_{hi}/D_{0i} = 2\xi_h^{(i)}/CK\chi_{\bar{h}} \tag{3}$$

and

$$D_{0i} = D_0^{(a)}, \quad D_{hi} = c^{(i)}D_0^{(a)}, \tag{4}$$

where $D_0^{(a)}$ denotes the amplitude of the incident wave.

The second part of the crystal is shifted with respect to the first (Authier, 1968) by the fault vector $\mathbf{f}$ and the dielectric susceptibility in region II is

$$\chi' = \sum \chi_h'(-2\pi i\mathbf{h}\cdot\mathbf{f}) \tag{5}$$

with

$$\chi_h' = \chi_h\exp(2\pi i\mathbf{h}\cdot\mathbf{f}), \quad \chi_{\bar{h}}' = \chi_{\bar{h}}\exp(-2\pi i\mathbf{h}\cdot\mathbf{f}), \tag{6}$$

where $\mathbf{h}$ is the reciprocal-lattice vector.

The one wave field excited in the first region (region I) of the crystal is split by the stacking fault into reflected and transmitted waves. Behind the fault plane (region II), these two waves excite four new wave fields. The fifth wave field in region II is excited by the incident wave. These five wave fields correspond to the two wave points situated on the normal to the fault plane. One of these points coincides with the wave point excited in the first region.

The rôle of absorption is very important and it causes some difficulty in the treatment based on the application of plane-wave dynamical theory. The attenuation of crystalline waves is described by the imaginary part of wave vectors and the interference components coming from the imaginary parts of the coordinates $\xi_{0,h}$ are determined by the continuity relation at the entrance surface. In an absorbing crystal, the waves created by decomposition of the wave fields at the plane obstacle, which is not parallel to the entrance surface, have variable amplitudes along the obstacle. In various applications of dynamical theory, they are still treated as plane waves, especially if phenomena along the wave vector are considered. It is, however more complicated to write the continuity relation between the imaginary parts of the wave vectors in the two regions of the crystal, similar to that on the entrance surface. This difficulty appears in the total reflection range, where the imaginary parts of the wave vectors are dominant; and it is difficult to treat the beam passing through the stacking fault as a plane wave. For this reason, we do not apply the present theory to the total reflection range. On the other hand, no fringes were observed experimentally in this region.

Including absorption requires appropriate calculation of the imaginary parts of the wave vectors induced by the wave fields decomposed at the fault plane. In particular, the imaginary parts of the wave vectors corresponding to the initially induced wave point cannot be approximated in region II by those from region I. In order to find the coordinates of the wave points with the correct imaginary parts, we first found the deviations from the Bragg angle of the waves created by the decomposition of the wave field in the fault plane. By some geometrical considerations, which may be found from Figs. 2 and 3, these deviations are:
for the forward diffracted wave:

$$\Delta\Theta'_{0i} = \Delta\Theta + \Re(\xi_0^{(i)}/K + \tfrac{1}{2}\chi_0)\sin\alpha/\gamma_0\gamma'_0; \quad (7)$$

for the reflected wave:

$$\Delta\Theta'_{hi} = -(\gamma'_0/\gamma'_h)\Delta\Theta'_{0i}. \quad (8)$$

The direction cosines of the reflected and transmitted waves with respect to the normal to the fault plane are now

$$\gamma'_0 = \sin(\alpha + \varphi - \Theta) \quad \text{and} \quad \gamma'_h = \sin(\alpha + \varphi + \Theta). \quad (9)$$

In the above formulae, φ is the inclination of the reflecting planes to the surface and α is the inclination of the stacking fault to the surface, with the positive direction marked in Fig. 3. In Fig. 2, $\Delta\Theta'_{0i} = \overline{MP'}/K$ and $\Delta\Theta'_{hi} = \overline{MQ'}/K$. In the situation actually shown, $\Delta\Theta'_{0i}$ is negative. The directions of the incident and back-reflected waves correspond to $\overline{PO}$ and $\overline{QH}$, respectively.

We can now find the complete expressions for the coordinates of the wave points using the normal formulae of dynamical theory in the Laue case. Here, the subscripts in parentheses denote the exciting wave.

$$\xi_{0i(0i)} = -\tfrac{1}{2}|C|K(\gamma'_0/\gamma'_h)^{1/2}(\chi'_h\chi'_{\bar{h}})^{1/2} \times [y' \pm (y'^2+1)^{1/2}], \quad (10)$$

where the new variable y' corresponds to the Laue-case diffraction in region II with the deviation from the Bragg angle given by $\Delta\Theta'_{0i}$:

$$y' = -[\sin 2\Theta\Delta\Theta'_{0i} + \tfrac{1}{2}\chi'_0(1-\gamma'_h/\gamma'_0)] \times [|C|(\gamma'_h/\gamma'_0)^{1/2}(\chi'_h\chi'_{\bar{h}})^{1/2}]^{-1}. \quad (11)$$

The remaining coordinates of the wave points excited by the forward-directed wave may be written

$$\xi_{hi(0i)} = K^2\chi'_h\chi'_{\bar{h}}C^2/4\xi_{0i(0i)} \quad (12)$$

$$\xi_{0j(0i)} = -(\gamma'_0/\gamma'_h)\xi_{hi(0i)} \quad (13)$$

$$\xi_{hj(0i)} = -(\gamma'_h/\gamma'_0)\xi_{0i(0i)}. \quad (14)$$

$j = 1,2$; $i \neq j$ and the indices of the incident wave (in parentheses) are $i = 1$ for $\Re y < -1$ and $i = 2$ for $\Re y > 1$.

The coordinates of the wave points induced by the reflected wave can now be found similarly by noting that the reflected wave can be treated as the incident wave for the $-\mathbf{h}$ diffraction vector with the deviation from the Bragg angle $\Delta\Theta'_{hi}$. Then the required coordinates may be found from those corresponding to the above-mentioned case after interchanging the subscripts indicating the reflected and incident beams.

$$\xi_{hi(hi)} = -\tfrac{1}{2}|C|K(\gamma'_h/\gamma'_0)^{1/2}(\chi'_h\chi'_{\bar{h}})^{1/2} \times [y_h \pm (y_h^2+1)^{1/2}], \quad (15)$$

where the new variable y_h corresponds to the deviation from the Bragg angle $\Delta\Theta'_{hi}$:

$$y_h = -[\sin 2\Theta\Delta\Theta'_{hi} + \tfrac{1}{2}\chi'_0(1-\gamma'_0/\gamma'_h)] \times [|C|(\gamma'_0/\gamma'_h)^{1/2}(\chi'_h\chi'_{\bar{h}})^{1/2}]^{-1}. \quad (16)$$

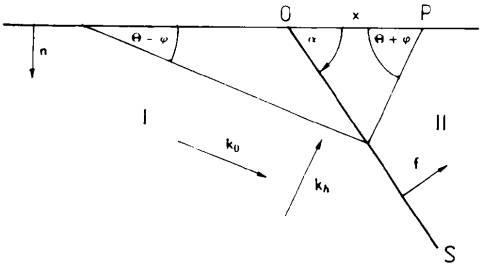

Fig. 3. The geometrical relation of the stacking fault in real space (OS – its intersections with the plane of diffraction). The arrow indicates the positive direction of the angle α.

Hence,

$$\xi_{0i(hi)} = K^2\chi'_h\chi'_{\bar{h}}C^2/4\xi_{hi(hi)} \quad (17)$$

$$\xi_{hj(hi)} = -(\gamma'_0/\gamma'_h)\xi_{0i(hi)} \quad (18)$$

$$\xi_{0j(hi)} = -(\gamma'_h/\gamma'_0)\xi_{hi(hi)}. \quad (19)$$

$j = 1, 2$; $i \neq j$ and the indices of the incident wave (in parentheses) are $i = 1$ for $\Re y < -1$ and $i = 2$ for $\Re y > 1$.

We can now list the four amplitudes of the waves in the diffracted beam, contributing to the Bragg–Laue-case stacking-fault image. For the waves excited by the forward-diffracted wave, the amplitudes $D_{hj(0i)}$ are given by

$$D_{h1(0i)} = D_0^{(a)}(2/K\chi'_{\bar{h}}C) \times [\xi_{01(0i)}\ \xi_{02(0i)}/(\xi_{02(0i)} - \xi_{01(0i)})] \quad (20)$$

$$D_{h2(0i)} = -D_{h1(0i)}, \quad (21)$$

where in region II the $c'^{(a)}$ has a different phase:

$$c'^{(a)} = \exp(2\pi i\mathbf{h}\cdot\mathbf{f}). \quad (22)$$

The amplitudes of the wave excited by the reflected wave may be written as

$$D_{h1(hi)} = D_0^{(a)}c'^{(a)}\xi_{h2(hi)}/(\xi_{h2(hi)} - \xi_{h1(hi)}) \quad (23)$$

$$D_{h2(hi)} = -D_{h1(hi)}. \quad (24)$$

In region II, we also have one wave field excited by the incident wave. This has again the same wave point as the wave field excited in the first region but the diffracted wave has a different phase,

$$D'_{hi} = D_0^{(a)}c'^{(a)} = D_{hi}\exp(2\pi i\mathbf{h}\cdot\mathbf{f}). \quad (25)$$

For calculation of theoretical images, we present the resultant amplitude of the diffracted beam as a function of the distance from the stacking-fault outcrop O (Fig. 3) along the surface x in the following way with the accuracy to a common phase factor:

$$\begin{aligned} D_h^{(a)}(x) = {} & [D_{hj(0i)} + D_{hj(hi)}]\exp\{-2\pi[\Im k_{hj(0i)} \\ & + \Im k_{0j}(\gamma_h/\gamma_0)](x\sin\alpha/\gamma'_h)\} \\ & \times \exp[2\pi i\Re k_{0j(0i)}(x\sin\alpha/\gamma'_h)] \\ & + ([D_{hi(0i)} + D_{hi(hi)}]\exp\{-2\pi[\Im k_{hi(0i)} \\ & + \Im k_{0i}(\gamma_h/\gamma_0)](x\sin\alpha/\gamma'_h)\} + D'_{hi}) \\ & \times \exp[2\pi i\Re k_{0i(0i)}(x\sin\alpha/\gamma'_h)] \end{aligned} \quad (26)$$

with $i = 1$ for $\Re y > 1$, $i = 2$ for $\Re y < -1$ and $j \neq i$ $(j = 1, 2)$.

In the above formula, we used the imaginary part of the wave vectors to calculate the effect of attenuation of the waves reaching the point P in Fig. 3. The real and imaginary parts of wave vectors can be found from calculated *Resonanzfehler* using the relation

$$k_{0,h(I)} = \xi_{0,h(I)} + K + \tfrac{1}{2}K\chi_{0,h(I)}, \quad (27)$$

where (I) denotes different possible extension of indices.

3. Numerical calculations

The above theory provided the basis for performing the calculations of theoretical images using appropriate computer programs. The relatively simple analytical formulae and the one-dimensional character of the problem allowed for calculation of both plane-wave theoretical images and integrated images taking into account the finite divergence of the beam existing in real experiments. The results were either plotted as a graph or presented in the form of a simulation of the topographic image.

4. Experimental

The sample was a 0.7 mm thick slab cut from a truncated octahedral diamond using a laser saw and polished. It was chosen from a number of synthetic diamonds with artificially introduced surfaces along (100) planes that we have examined. The chosen sample, together with a neighbouring sample cut from the same diamond, was also widely studied with various X-ray topographic methods, optical methods and cathodoluminescence topography (Wierzchowski, Moore, Makepeace & Yacoot, 1991).

The good-quality fringe patterns in the Bragg-case images of the stacking faults were obtained with a synchrotron X-ray source. The synchrotron double-crystal experiments were preceded by some experiments with a conventional X-ray source which provided some traces of the fringes. The experiments were performed using Cu $K\alpha_1$ radiation in an arrangement with the $1\bar{4}32$ reflection from a quartz monochromator and various diamond reflections of 311 type. The matching of these two reflections is very good and the broadening of the rocking curve by spectral dispersion should theoretically be close to 0.5″.

The synchrotron experiments were performed at station 7.6 of the SERC Daresbury Laboratory storage ring. In these experiments, we attempted to reconstruct the situation of the conventional source experiment, but to obtain much better visibility of fringes due to the better spatial resolution and smaller influence of spectral dispersion.

Owing to the 80 m distance of the experimental arrangement from the tangent point of the synchrotron source, it was possible to accept a much worse matching from the reflections on the monochromator and diamond investigated. We used there the 511 reflection from a (111)-oriented silicon monochromator to match the 311 reflection from the diamond slab. We chose the

reflections that provided the best visibility of stacking faults, as had been found in the conventional source experiments. The arrangement selected 1.54 Å radiation, the same wavelength as Cu $K\alpha_1$. In the case of a (100)-oriented surface, the inclination of the (311) reflecting planes φ is close to 25°, while the inclination of the (111) stacking fault α is close to 54°.

The initial collimation of the beam was close to 1″ and it is five times smaller than the width of the rocking curve for the asymmetrical reflection used. In the first approximation, the divergence of the probe beam is further reduced by the asymmetry factor. Taking into account the effects due to the imperfect fitting of the lattice spacings, we evaluated the probe beam width as approximately 0.2″. The effective divergence of the probe beam both in synchrotron and conventional source experiments could be increased by thermal and mechanical instabilities. That effect was monitored by intensity measurements and should not exceed 0.1″. By placing the nuclear emulsion plate at a distance less than 3 cm, we found it was possible to obtain a spatial resolution better than 1 μm. The topographs were exposed on Ilford L4 nuclear emulsions of thickness 25 μm, in a series containing more than 20 exposures on each plate, at various angles near the peak reflection. To reduce thermal instabilities, the monochromator was constantly illuminated by the beam and a shutter between the diamond and plate was operated remotely, as was the movement of the cassette. Each series was taken with 0.5″ angular adjustment to the sample between exposures, and with prolongation of the exposure time on the tails of the rocking curve.

Owing to the domination of the σ polarization in the incident beam and because successive reflections had Bragg angles close to 45°, we may consider the present images as fully corresponding to σ polarization.

Comparative studies of stacking-fault images were performed in another synchrotron double-crystal arrangement with the 004 symmetrical Bragg-case reflection matched by the $53\bar{1}$ asymmetrical reflection from the same monochromator. The same Bragg angle close to 45° was used, selecting 1.35 Å radiation.

5. Results and discussion

5.1. *Appearance of the fringes*

The details of the dislocation and growth-sector structure of the sample have been described in a separate paper (Wierzchowski *et al.*, 1991). It should be noted that the distribution of dislocations in this crystal was not uniform and that we revealed stacking faults by various topographic methods. Many of these stacking faults outcropped onto the artificially introduced surfaces. It was very difficult to obtain fringe patterns associated with a stacking fault, except in the case of synchrotron double-crystal topographs.

The surface investigated in the present topographs was relatively far from the seed and bounded the most perfect region of the diamond. Also, the pattern of growth sectors was relatively simple, containing a relatively large central (100) growth sector surrounded by four large {111} growth sectors separated from each other by {110} sectors and from the central sector by narrow {311} sectors.

The configuration of stacking faults and other defects near the investigated surfaces may be deduced from the single-crystal back-reflection topographs in the 311 reflection of Cu $K\alpha_1$, shown in Fig. 4. The single-crystal method is less sensitive and reveals only weak contrast on the growth-sector boundaries. The dislocations are revealed with much lower contrast but those near the stacking faults are quite intense and allow one to follow the location of stacking faults quite well. No fringes obviously occur in the single-crystal topographs.

It should be noted that the stacking faults obeyed the extinction of contrast $\mathbf{h} \cdot \mathbf{f} = m$, where m is an integer and $\mathbf{f}$ is the fault vector. In crystals with the diamond structure, $\mathbf{f}$ is either $\frac{1}{3}\langle 111\rangle$ for an intrinsic type of stacking fault or $\frac{2}{3}\langle 111\rangle$ for the theoretically possible extrinsic type of stacking fault. The fault vector is perpendicular to the {111} fault plane. We were able to confirm these extinction rules using various topographic methods. A particular stacking fault is not visible in two of the four 311-type reflections, when it intersects the plane of diffraction parallel to the surface.

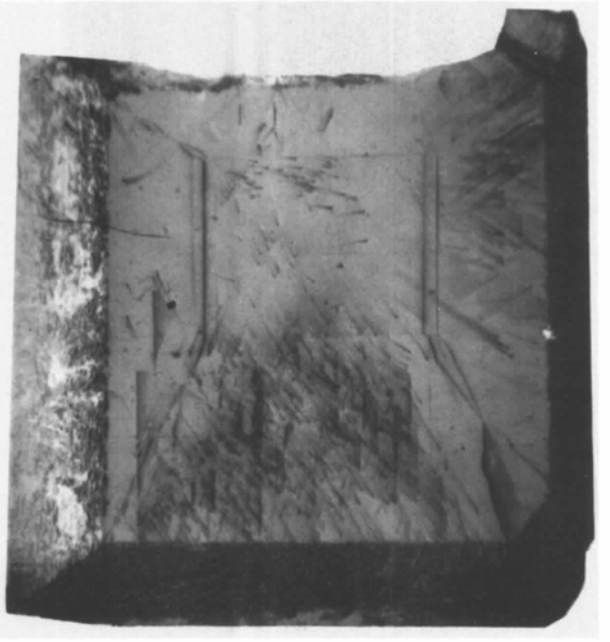

Fig. 4. The 311 Cu $K\alpha_1$ single-crystal back-reflection projection topograph, presenting the configuration of stacking faults close to the investigated surface of the slab cut from the De Beers synthetic octahedral diamond. The plane of diffraction is located horizontally.

(*a*)

(*b*)

(*c*)

(*d*)

Fig. 5. The series of four double-crystal Bragg–Laue images of a stacking fault, taken with the 511_{Si},$-311_{\diamond}$ synchrotron arrangement with 1.54 Å radiation. The topographs are ordered in increasing angle of incidence, (*a*) and (*b*) on the low-angle tail and (*c*) and (*d*) on the high-angle tail of the rocking curve. The arrows mark the detail where the behaviour of the first fringe is in the best agreement with the theory for an assumed intrinsic type of stacking fault. Projection of the diffraction vector, in each case, is horizontal and pointing to the left. The image width is 900 μm.

Well resolved interference fringes from stacking faults and dislocations were obtained with the 511_{Si},$-311_{\diamond}$ synchrotron arrangement, selecting 1.54 Å radiation.

We observed a characteristic change in the periodicity of fringes; they become more compressed further from the peak. The fringes vanished close to the peak, corresponding to the total reflection range. This was also true of the fringes in the Bragg–Bragg case. In some cases, we observed bending of fringes close to the dislocations bounding the faults. The appearance of the fringes is shown in Fig. 5 showing their images in four angular settings – two on each tail of the rocking curve further from and closer to the maximum. The figure presents the images of the two stacking faults in the Bragg–Laue case with the most visible fringe pattern.

Good visibility of interference fringes was due both to the spatial resolution being better than 1 μm and to the very good combination of small incident-beam divergence (of the order of 0.2″) with a relatively wide intrinsic rocking curve (3.1″) for the asymmetrical 311 diamond reflection. The second factor partly accounted for the almost complete invisibility of fringes in the 531_{Si},$-400_{\diamond}$ synchrotron arrangement with 1.35 Å radiation. In the last case, the divergence of the incident beam was similar but the width of the rocking curve was twice as small. The relatively wide rocking curve also had the effect of decreasing the influence of inclusions and other defects, thus causing the crystal to behave more like a perfect one.

5.2. *Correspondence of experimental and theoretical images*

We obtained good correspondence between the observed fringe patterns at the stacking faults and the theoretical predictions presented in the former part of this paper. The theoretical intensity distributions for intrinsic and extrinsic types of stacking fault corresponding to the experimental Bragg–Laue images shown in Fig. 5 are presented in Figs. 6 and 7. In these figures, we present both theoretical images for an incident plane wave and for an incident wave with 0.3″ divergence. The plots were calculated for the angular positions $\Delta\Theta$ equal to 5.5, 6.8, 10.3 and 11.5″, corresponding to values of $\Re y$ of 2.0, 1.2, −1.1 and 1.9, respectively. All diagrams were plotted to have their maximal value at the same level while in fact the corresponding maximal values are in the ratio 1 : 3.2 : 3.8 : 1.2.

The corresponding angular position of the experimental topographs seem to be in rough agreement with the values of the plots, in particular the angular distance between the topographs 5(*a*) and (*b*) is close to 1.5″ and similarly between the topographs 5(*c*) and (*d*), and the accuracy of these estimates is close to 0.3″. We also notice a systematic difference in periodicity of the two stacking faults shown in the topographs, owing to a local difference in the region of the rocking curve.

The different types of stacking fault cause a small difference in the theoretical image close to the outcrop of the stacking fault (giving a difference in the starting phase of oscillations) and the image is different on the two sides of the rocking curve. These features provide the possibility of identification of stacking-fault type. The experimental topographs are in good agreement with theory and correspond better to those calculated for the intrinsic type of stacking fault. It may be easily found from (25) that the phases of all five component waves are differently dependent on the fault vector for $x = 0$.

We have found that the main period of the interference fringes visible in the theoretical images of stacking faults is the same as that in the integrated images along a dislocation line at the same angular settings. The formation of fringes in both cases is similar, as the same single field is decomposed by a similarly situated obstacle and new wave fields with tie-points located on the normal to the obstacle are formed. There are some differences caused by different wave amplitudes corresponding to these wave fields; a more exact model has been discussed by Gronkowski & Malgrange (1984) but the main period Δ_T is due to the difference of the wave vectors corresponding to these two points. It may be written by the formula

$$\Delta_T = \gamma'_h/(\sin\alpha|k_{h1} - k_{h2}|), \tag{28}$$

where, as previously, α is the inclination of the fault plane. According to (10) and (15), we can write

$$\Delta_T = \gamma'_h/[\sin\alpha|CK(\gamma'_0/\gamma'_h)^{1/2}(\chi'_h\chi'_{\bar{h}})^{1/2} \times (y'^2 + 1)^{1/2}|]. \tag{29}$$

The period is here dependent on the real parts of the wave vectors, which are themselves dependent only on the location of the obstacle; and it is not important in the above formula whether we take the wave points excited by the reflected or transmitted beam behind the fault plane. The formula was fulfilled in all calculated plots.

It should be noted that the Bragg-case images are dependent on the stacking-fault type even at very low absorption. This is different from the case of plane-wave Laue-case images. In this last case, the two wave points are excited in the first part of the crystal and the dependence on the fault vector coming from the field subsequently generated from these two wave fields is compensated. The dependence on the fault type appears when the crystal is significantly absorbing (Kato, 1974).

No significant decrease in visibility of the fringes in both theoretical and experimental images was observed on the high-angle tail of the rocking curve where the Borrmann effect was negative. The negative Borrmann effect on the high-angle side causes a faster decrease of maximal amplitude with distance from the outcrops

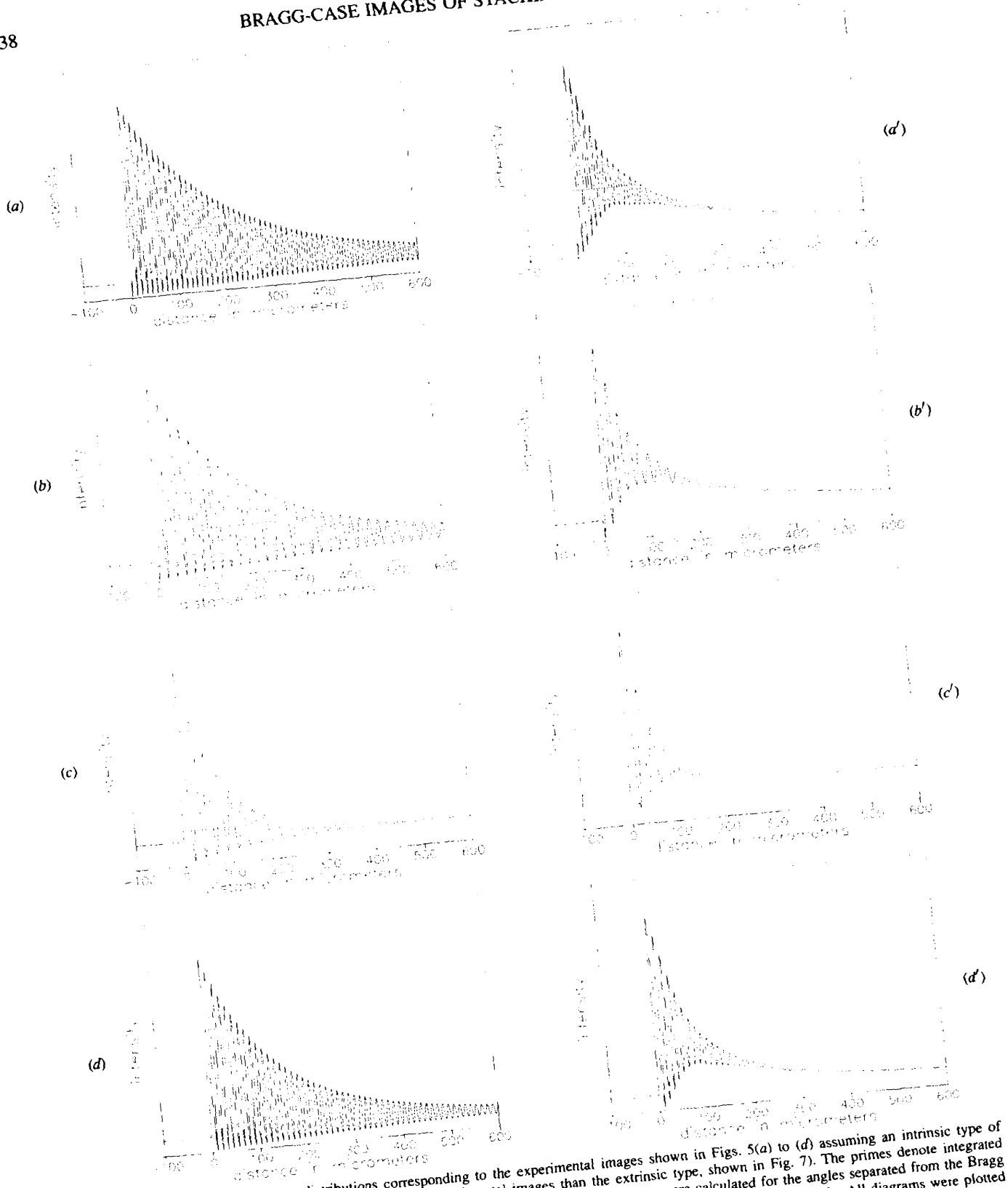

Fig. 6. The theoretical intensity distributions corresponding to the experimental images shown in Figs. 5(*a*) to (*d*) assuming an intrinsic type of stacking fault (which more closely resembles the experimental images than the extrinsic type, shown in Fig. 7). The primes denote integrated images, taking into account the 0.3″ divergence of the incident beam. The distributions were calculated for the angles separated from the Bragg angle at $\Delta\Theta$ equal to 5.5, 6.8, 10.3 and 11.5″, corresponding to values of $\Re y$ of 2.0, 1.2, −1.1 and 1.9, respectively. All diagrams were plotted to have their maximal value at the same level and the corresponding maximal values are in the ratio 1 : 3.2 : 3.8 : 1.2.

than that observed on the low-angle side for the positive Borrmann effect.

In the case of theoretical profiles corresponding to the topographs taken using the $511_{Si},-311_{\diamond}$ arrangements, the including of beam divergence with a realistic value of 0.3″ caused increasing smearing of successive fringes. It was connected with a characteristic increase of the background. This feature was well visible in experimental topographs. The integrated images marked by letters with primes are in much better agreement with experimental patterns than those for the plane wave.

6. Concluding remarks

The Bragg-case images of stacking faults exhibiting distinct interference fringes were obtained in a slab cut from a large synthetic diamond of truncated octahedral habit with the use of double-crystal topographic methods using a synchrotron X-ray source. The best visibility of fringes was obtained using the $511_{Si},-311_{\diamond}$ arrangement owing to both the very good spatial resolution and the good combination of small divergence of the incident beam and the relatively wide rocking curve.

The fringe patterns were strongly dependent on the angular position on the rocking curve. They were invisible in the peak regions and became more closely spaced further from the peak.

The application of plane-wave theory for the diffraction from stacking faults has been discussed. We obtained a good correspondence between theoretical and experimental patterns, especially after taking into account the finite divergence of the incident beam.

The starting sequence of the theoretical images close to the stacking-fault outcrop was found to depend on the type of stacking fault and this sequence was also dependent on the side of the rocking curve. This provided the possibility of identification of the stacking-fault type, different from the case of transmission plane-wave topographs for low absorbing crystals. We confirmed the intrinsic character of the stacking faults observed.

The authors are greatly indebted to the Science and Engineering Research Council and to De Beers Industrial Diamond Division (Pty) for financial support. They would also like to thank Professor A. R. Lang FRS (University of Bristol) for his helpful advice, Mr R. Waggett for taking part in some of the experiments and the referee for constructive comments.

Fig. 7. The theoretical intensity distributions corresponding to the experimental images shown in Figs. 6(*b*) and (*c*) assuming an extrinsic type of stacking fault. The primes denote the integrated images, taking into account the 0.3″ divergence of the incident beam.

References

AUTHIER, A. (1968). *Phys. Status Solidi*, **27**, 77–93.
BEDYŃSKA, T., BUBÁKOVÁ, R. & ŠOUREK, M. (1976). *Phys. Status Solidi A*, **36**, 509–516.
BUBÁKOVÁ, R. & ŠOUREK, M. (1976). *Phys. Status Solidi A*, **35**, 55-64.
BURNS, R. C., ROBERTSON, S. H. & KEDDY, R. J. (1993). In *The Physical Properties of Natural and Synthetic Diamonds*, edited by J. E. FIELD. New York: Academic Press.
GRONKOWSKI, J. (1980). *Phys. Status Solidi A*, **57**, 105–112.
GRONKOWSKI, J. & MALGRANGE, C. (1984). *Acta Cryst.* A**40**, 515–522.
JIANG, S.-S. & LANG, A. R. (1983). *Proc. R. Soc. London Ser. A*, **388**, 249–271.
KATO, N. (1974). *X-ray Diffraction*, by L. V. AZÁROFF, R. KAPLOW, N. KATO, R. J. WEISS, A. J. C. WILSON & R. A. YOUNG, chs. 3–5, pp. 176–438. New York: McGraw-Hill.
KATO, N., USAMI, K. & KATAGAWA, T. (1967). *Adv. X-ray Anal.* **10**, 46–66.
KOWALSKI, G. & LANG, A. R. (1986). *J. Appl. Cryst.* **19**, 224–228.
KOWALSKI, G., LANG, A. R., MAKEPEACE, A. P. W. & MOORE, M. (1989). *J. Appl. Cryst.* **22**, 410–430.
STRONG, H. M. & WENTORF, R. H. JR (1972). *Naturwissenschaften*, **59**, 1–7.
WIERZCHOWSKI, W. & MOORE, M. (1992). *Acta Phys. Pol.* **82**, 185–191.
WIERZCHOWSKI, W., MOORE, M., MAKEPEACE, A. P. W. & YACOOT, A. (1991). *J. Cryst. Growth*, **114**, 209–227.

Acta Cryst. (1995). A**51**, 840–845

A Tangent Formula Derived from Patterson-Function Arguments. III. Structure Determination of Zeolitic and Layered Materials from Low-Resolution Powder Diffraction Data

BY J. RIUS, J. SAÑÉ AND C. MIRAVITLLES

Institut de Ciència de Materials de Barcelona (CSIC), Campus de la UAB, 08193-Cerdanyola, Catalunya, Spain

AND H. GIES, B. MARLER AND U. OBERHAGEMANN

Institut für Mineralogie, Ruhr-Universität Bochum, D-44780 Bochum, Germany

(*Received* 17 *December* 1994; *accepted* 1 *May* 1995)

Abstract

The viability of solving the structure type of zeolitic and layered materials applying multisolution direct methods to low-resolution (~2.2 Å) powder diffraction data is shown. The phases are refined with the tangent formula derived from Patterson-function arguments [Rius (1993). *Acta Cryst.* A**49**, 406–409] and the correct phase sets are discriminated with the conventional figures of merit. The two test examples presented are (*a*) the already known tetragonal zeolite ZSM-11 (space group $I\bar{4}m2$) at 2.3 Å resolution and (*b*) the hitherto unknown layer silicate RUB-15 (*Ibam*) at 2.2 Å resolution. In both cases, the tetrahedral Si units appear as resolved peaks in the Fourier maps computed with the phases of the highest-ranked direct-methods solutions.

1. Introduction

To understand the physical and chemical properties of zeolitic and layered materials, and to retrieve valuable information about the synthesis mechanisms, a knowledge of their crystal structures is a prerequisite. When no sufficiently large single crystals are available, the crystal structure must be solved from very limited experimental data, such as powder diffraction, in combination with model building and other experimental techniques, *e.g.* ^{29}Si MAS NMR and electron diffraction. In recent years, the easier access to synchrotron X-ray sources, the existence of programs for extracting integrated intensities from high-resolution powder patterns (*e.g.* Pawley, 1981; Baerlocher, 1990) as well as improved computing facilities have rendered possible the *ab initio* solution of some highly crystalline zeolite-like compounds by direct methods (*e.g.* Rudolf, Saldarriaga-Molina & Clearfield, 1986; McCusker, 1988). The application of alternative methods, such as the direct interpretation of the Patterson function, is hampered by the relatively large number of tetrahedrally coordinated atoms (hereafter referred to as *T*) and by the fact that *T* atoms, *e.g.* Si, are not very much heavier than O atoms, so that the *T*–*T* interatomic peaks cannot be easily identified in the Patterson map. Other alternatives such as the application of Patterson search techniques, although viable (Rius & Miravitlles, 1988; Gies & Rius, 1995), are far from trivial.

In many cases, zeolites crystallize as microcrystalline powders of poor crystallinity. The use of synchrotron radiation for these cases is less suitable. In these materials, peak broadening due to the sample often outweighs instrumental broadening so that only the low-resolution intensities can be extracted reliably from their powder patterns. This imposes serious limitations on the applicability of direct methods. These limitations have